A QMU Lagrangian for the Photoelectric Effect: Banded Photons, Dynamic Photon Number, and rmfd Tests

David W. Thomson III[1]

[1]Quantum AetherDynamics Institute

September 27, 2025

Abstract

We present a QMU-closed Lagrangian for the photoelectric effect that reproduces the Einstein [1, 2] line within the QMU ledger, elevates the photon-number density $\widehat{n}_\gamma$ to a dynamical field with axiomatic continuity, and implements a banded-photon ontology in which emission populates a Compton-following conical band[3, 4] (a ring on the observation sphere) rather than an isotropic lobe [1, 2, 3, 4]. The total Lagrangian (CEPL) enforces $\partial_\tau \widehat{n}_\gamma + \boldsymbol{\nabla}_\xi \cdot \widehat{\mathbf{S}}_\gamma = \mathcal{X}_\gamma$ and encodes the band via a kernel $\mathcal{K}_{\rm band}$ whose half-angle obeys cone rules (C1)–(C2). Three falsifiable predictions follow: (P1) a universal near-threshold circular-dichroism amplitude, (P2) an rmfd-coupled work-function shift controlled by independently calibrated surface-ledger parameters, and (P3) a polarization-ring front–back asymmetry unique to two-channel interference [5, 6]. A finite response bound (P4) emerges from first-order QMU time evolution and is testable against attosecond photoemission timing [7, 8]. Appendix A derives the "cardioid on a cone" imprint from a constant-pitch loxodromic spin path by stationary phase (whose instantaneous cardioid time-averages to the observed annular band) [9]. Calibration protocols rely on speckle-based roughness/slope, Kerr-based magnetic contrast, and fluctuation–dissipation readouts in QMU units [10, 11, 12, 13].

1 Introduction

Key departures from standard theory. (1) *Dual-charge channels:* light–matter interaction runs through both electric (e^2) and magnetic ($e_{\rm emax}{}^2$) distributed charges in APM. (2) *Banded emission:* photons are emitted into a Compton-following cone (ring on the observation sphere), not isotropically. (3) *Dynamic photon number:* the photon-density $\widehat{n}_\gamma$ is a fundamental, continuous field with its own continuity equation.

A key claim of this work—the "cardioid on a cone" emission geometry—is not assumed but derived from the constant-pitch loxodromic spin path of the Aether unit; Appendix A sketches the stationary-phase selection of the cone and shows that the azimuthal Jacobian is first harmonic, making the iso-intensity contour a cardioid. Sub-cycle precession time-averages this imprint into the observed annular band (Prediction P3 makes it directly testable with time-gated or azimuth-restricted readouts).

2 QMU ledger and ontology

Action, energy, volume (QMU).

$$\boxed{\text{angm} \equiv m_\text{e}\,{\lambda_\text{C}}^2\,F_\text{q}}, \qquad \boxed{\text{enrg} \equiv \text{angm}\,F_\text{q} \;=\; m_\text{e}\,{\lambda_\text{C}}^2\,{F_\text{q}}^2}, \qquad \boxed{\text{volm} \equiv {\lambda_\text{C}}^3}.$$

Charge-channel couplings.

$$g_\text{e} = \frac{e^2}{\text{angm}}, \qquad g_\text{m} = \frac{{e_\text{emax}}^2}{\text{angm}}, \qquad \eta_\text{c} = \frac{e^2}{{e_\text{emax}}^2}. \tag{1}$$

Kinematics and drive.

$$\boldsymbol{\xi} = \frac{\mathbf{r}}{\lambda_\text{C}}, \quad \tau = F_\text{q} t, \quad u = \frac{\nu}{F_\text{q}}, \quad \kappa = \frac{K}{\text{enrg}}, \quad \Phi = \frac{\phi}{\text{enrg}}. \tag{2}$$

Speed of photons and rotating magnetic field.

$$\boxed{c = \lambda_\text{C}\,F_\text{q}}, \qquad \boxed{\text{rmfd} \equiv A_\text{u}}.$$

Here c is the photon speed, and rmfd equals A_u (APM rotating magnetic field). In dimensionless equations we scale physical fields by A_u; see §5.

Light ledger (phtn, ligt, ocmp).

$$\boxed{\text{phtn} \equiv \text{angm}\,c}, \qquad \boxed{\text{ligt} \equiv \text{phtn}\,F_\text{q}}, \qquad \boxed{\text{ocmp} \equiv \frac{1}{\text{ligt}}}.$$

Thus phtn $=$ angm c, ligt $=$ phtn F_q, and ocmp $= 1/$ligt.

Photon counting and throughput (dimensionless).

$$\widehat{n}_\gamma \equiv \frac{\mathbf{E}_\text{e}^2 + \mathbf{B}_\text{e}^2 + \mathbf{E}_\text{m}^2 + \mathbf{B}_\text{m}^2}{2\,u}, \qquad \widehat{\mathbf{P}} \equiv \mathbf{E}_\text{e} \times \mathbf{B}_\text{e} + \mathbf{E}_\text{m} \times \mathbf{B}_\text{m}, \qquad \widehat{\mathbf{S}}_\gamma \equiv \frac{1}{2\,u}\,\widehat{\mathbf{P}}.$$

Banded-photon origin (APM geometry). The banded-photon ontology stems from the loxodromic geometry of the electron's Aether unit: emission aligns with the tangent cone of the intrinsic spin-path, producing a *ring* at half-angle ϑ_C about the director $\widehat{\mathbf{d}}$. The anchored cone and its multi-cycle averaged band are illustrated in Figure 1.

From a cardioid on the cone to banded rings (detector projection)

Instantaneous picture (cardioid on an anchored cone). At any given QMU tick, the emission lives on a conical sheet at half-angle ϑ_C about the director $\widehat{\mathbf{d}}$. The angm ledger density around the cone's azimuth φ carries a mild cardioid modulation $\mathcal{C}_\text{card}(\varphi) = 1 + \epsilon\,[1 - \cos(\varphi - \varphi_0)]$. This instantaneous geometry is what is drawn in Figure 8.

How rings appear on a detector. Let a flat detector (or the equatorial plane) intersect the outward-moving conical sheet. Distance along the cone s maps to detector radius $r = s \sin\vartheta_\text{C}$. A pulse envelope $g(s - ct)$ therefore yields a ring at $r = ct \sin\vartheta_\text{C}$. Over many cycles, the detector

integrates around φ so the cardioid averages to a circular band; residual azimuthal structure only survives in time-gated or azimuth-restricted readouts:

$$I(r) \;\propto\; \int_0^{2\pi} \underbrace{\mathcal{K}_{\rm band}(\widehat{\mathbf{r}}_\xi;\widehat{\mathbf{d}},\vartheta_{\rm C},\varsigma_{\rm C})}_{\text{cone ring}}\,\underbrace{\mathcal{C}_{\rm card}(\varphi;\varphi_0,\epsilon)}_{\text{cardioid imprint}}\, g\Big(\tfrac{r}{\sin\vartheta_{\rm C}}-ct\Big)\,\mathrm{d}\varphi.$$

This measured $I(r)$ is the time-averaged counterpart of the instantaneous ledger density $\mathcal{J}_\Omega(\widehat{\mathbf{r}}_\xi;\xi) = \widehat{\mathbf{r}}_\xi\cdot\widehat{\mathbf{S}}_\gamma$; the integration over many chronovibration cycles washes out the cardioid emboss into a uniform annulus, with residual azimuthal structure surviving only under time-gating or restricted φ acceptance.

This is the origin of the "banded rings" shown schematically in Figure 3.

Deterministic Aether-Ledger Interpretation. All "emission" statements are to be read as *deterministic transfers of angular momentum density* from the electron's Aether unit to surrounding Aether units. The Route B sector enforces exact continuity,

$$\partial_\tau \widehat{n}_\gamma + \boldsymbol{\nabla}_\xi\cdot\widehat{\mathbf{S}}_\gamma \;=\; \mathcal{X}_\gamma,$$

so $\widehat{n}_\gamma$ and $\widehat{\mathbf{S}}_\gamma$ are *ledger currents*, not probabilities and not particles in flight. A chronovibration tick $\Delta\tau = 1$ is the minimal update of this transfer (cf. P4). The geometric confinement to a cone is an *anchored projection* of the electron's cardioid surface into the surrounding Aether.

Cardioid ledger. Kinetic layers map to a geometric series of expanding concentric cardioids of velocity-squared (fig. 5) in the QMU ledger. (See Figure 8 for instantaneous geometry and Figure 3 for the ring-accumulation view.)

3 Lagrangian with dynamic photon number (Route B)

Electron sector and channels.

$$\mathbf{D} = \boldsymbol{\nabla}_\xi - i(g_{\rm e}\,\mathbf{a}_{\rm e} + g_{\rm m}\,\mathbf{a}_{\rm m}), \qquad D_\tau = \partial_\tau - i\,\varphi(\boldsymbol{\xi}). \tag{3}$$

Total (dimensionless) Lagrangian density per volm**.**

$$\boxed{\begin{aligned}\widehat{\mathcal{L}} = {}& \psi^\dagger\Big(i\,D_\tau - \Phi_s(\boldsymbol{\xi}) - \tfrac{1}{2}\,\mathbf{D}^2\Big)\,\psi \;+\; \chi_\Omega\,\boldsymbol{\Omega}\cdot(\psi^\dagger\boldsymbol{\sigma}\psi)\\ & + \tfrac{1}{2}\Big(\mathbf{E}_{\rm e}^2 - \mathbf{B}_{\rm e}^2\Big) \;+\; \tfrac{1}{2}\Big(\mathbf{E}_{\rm m}^2 - \mathbf{B}_{\rm m}^2\Big) \;+\; \lambda_\times\,\mathbf{E}_{\rm e}\cdot\mathbf{B}_{\rm m}\\ & - \lambda_{\rm cplg}\Big[\widehat{n}_\gamma - \tfrac{1}{2u}\,(\mathbf{E}_{\rm e}^2 + \mathbf{B}_{\rm e}^2 + \mathbf{E}_{\rm m}^2 + \mathbf{B}_{\rm m}^2)\Big]\\ & + \mu_\gamma\,\Big(\partial_\tau\widehat{n}_\gamma + \boldsymbol{\nabla}_\xi\cdot\widehat{\mathbf{S}}_\gamma - \mathcal{X}_\gamma\Big).\end{aligned}} \tag{4}$$

Exchange/source term and band kernel.

$$\mathcal{X}_\gamma \;=\; \Gamma_{\rm em}(u,\Phi;g_{\rm e},g_{\rm m},\lambda_\times)\,|\psi|^2\,\mathcal{K}_{\rm band}(\widehat{\mathbf{r}}_\xi;\widehat{\mathbf{d}},\vartheta_{\rm C},\varsigma_{\rm C}) \;-\; \Gamma_{\rm abs}(u,\Phi)\,|\psi|^2.$$

$$\mathcal{K}_{\rm band}(\widehat{\mathbf{r}}_\xi;\widehat{\mathbf{d}},\vartheta_{\rm C},\varsigma_{\rm C}) = \frac{1}{\sqrt{2\pi}\,\varsigma_{\rm C}}\,\exp\!\left(-\frac{\big[\arccos(\widehat{\mathbf{d}}\cdot\widehat{\mathbf{r}}_\xi)-\vartheta_{\rm C}\big]^2}{2\,\varsigma_{\rm C}^2}\right).$$

Cardioid imprint on the cone. To reflect the cardioid shape of the electron down the Aether unit's z axis, we modulate the ring by a cardioid factor around the azimuth φ measured in the band plane:

$$\mathcal{C}_{\rm card}(\varphi;\varphi_0,\epsilon) \;=\; 1+\epsilon\,[1-\cos(\varphi-\varphi_0)], \qquad 0\le\epsilon\ll 1.$$

The directional *ledger density* on a sphere of radius $\xi = r/\lambda_{\rm C}$ is then

$$\mathcal{J}_\Omega(\hat{\mathbf{r}}_\xi;\xi) \;\equiv\; \hat{\mathbf{r}}_\xi\cdot\widehat{\mathbf{S}}_\gamma(\xi,\hat{\mathbf{r}}_\xi) \;\propto\; \Gamma_{\rm em}\,\mathcal{K}_{\rm band}(\hat{\mathbf{r}}_\xi;\widehat{\mathbf{d}},\vartheta_{\rm C},\varsigma_{\rm C})\,\mathcal{C}_{\rm card}(\varphi;\varphi_0,\epsilon),$$

which is a deterministic *throughput* per solid angle, not a probability density. The δ-cone limit is recovered as $\sigma_{\rm C}\to 0$. *Instantaneous vs. time-averaged.* The instantaneous cardioid drawn on the cone (Figs. 8) time-averages, over chronovibration, to the annular band seen experimentally (Fig. 1); the unified φ-profile appears in Fig. 7.

Compton-following cone (testable rules).

$$\text{(C1)}\;\; 1-\cos\vartheta_{\rm C}=\frac{\chi_{\rm C}}{u}, \qquad \text{(C2)}\;\; 1-\cos\vartheta_{\rm C}=\frac{\chi_{\rm C}}{u-\Phi}.$$

Figure linkage. The cone half-angle $\theta_{\rm C}$ set by (C1)–(C2) is annotated in Figs. 1 and 8.

Cone Rule from Loxodromic Spin Geometry (Derivation Sketch)

Let the electron's intrinsic spin-path be a loxodrome on the $\lambda_{\rm C}$-scaled sphere, with unit tangent $\mathbf{t}(\tau)$ and constant pitch relative to the local azimuth. Emission extrema arise from stationary phase of the action density along the spin path. In QMU, the phase advance per tick is $\Delta\phi = \mathrm{angm}^{-1}\,\mathrm{enrg}\,\Delta\tau = \Delta\tau$ and the stationary-phase exit direction $\hat{\mathbf{r}}_\xi$ satisfies

$$\hat{\mathbf{r}}_\xi\cdot\mathbf{t}=\cos\vartheta_{\rm C}, \qquad 1-\cos\vartheta_{\rm C}=\frac{\chi_{\rm C}}{u}.$$

The $1/u$ scaling follows from matching the longitudinal phase gradient to the u-set photon ledger: higher u contracts the exit cone. This reproduces (C1); the near-threshold variant (C2) follows by replacing $u\to u-\Phi$ to include binding.

Foundational status. If a full loxodromic functional derivation is deemed out of scope, the band kernel $\mathcal{K}_{\rm band}$ and rule (C1) may be taken as an axiom grounded in APM geometry, with (C2) a near-threshold corollary. Both are explicitly testable via ring-resolved ARPES.

4 Derivation of Couplings from APM Geometry

Topological/electro-geometric ansatz. APM posits dual distributed charges with ratio $\eta_{\rm c} = e^2/{e_{\rm emax}}^2 = 8\pi\alpha$ and a canonical topological weight $\beta_0 = 1/(16\pi^2)$. Cross-channel effects scale with $\eta_{\rm c}\beta_0$.

Spin–rmfd coupling (dimensionless).

$$\boxed{\chi_\Omega \;=\; \eta_{\rm c}\,\beta_0 \;=\; \frac{\alpha}{2\pi}}$$

Electric–magnetic cross coupling.

$$\boxed{\lambda_\times \;=\; \eta_{\mathrm{c}}\,\beta_0 \;=\; \frac{\alpha}{2\pi}}$$

Photon–field coupling.

$$\boxed{\lambda_{\mathrm{cplg}} \;=\; 1}$$

Cone-rule constant.

$$\boxed{\chi_{\mathrm{C}} = 1}$$

5 Dimensionless normalization of rmfd

Let $\mathbf{\Omega}^{(\mathrm{phys})}$ denote the physical rotating magnetic field (rmfd) amplitude at the surface. We define the *dimensionless* drive vector by scaling with the APM rmfd ledger unit (rmfd $\equiv A_{\mathrm{u}}$):

$$\boxed{\mathbf{\Omega} \;\equiv\; \mathbf{\Omega}^{(\mathrm{phys})}/A_{\mathrm{u}}}.$$

The spin–rmfd term is then $\chi_\Omega\,\mathbf{\Omega}\cdot(\psi^\dagger\boldsymbol{\sigma}\psi)$, which is manifestly dimensionless. This justifies the appearance of "rmfd" effects *without* an explicit rmfd factor in $\widehat{\mathcal{L}}$: all amplitudes are pre-scaled by A_{u}.

Physical Origin and Control of rmfd

The rmfd ledger unit rmfd $\equiv A_{\mathrm{u}}$ defines the normalization; the *field itself* is the sum of independent contributions:

$$\mathbf{\Omega}^{(\mathrm{phys})} = \mathbf{\Omega}_{\mathrm{ext}} + \mathbf{\Omega}_{\mathrm{int}}.$$

External rmfd $\mathbf{\Omega}_{\mathrm{ext}}$ is generated in the lab by phase-shifted, orthogonal channel drives producing a controlled rotation at the surface; we report only the dimensionless amplitude $\mathbf{\Omega} = \mathbf{\Omega}_{\mathrm{ext}}/A_{\mathrm{u}}$. *Internal* rmfd $\mathbf{\Omega}_{\mathrm{int}}$ arises from prepared magnetic textures (domain precession, skyrmion gyration[6]) and is quantified by $\widehat{\sigma}_{\mathrm{mflx}}$ and $\widehat{g}_{\mathrm{mfxd}}$ (cf. §12). Predictions P2 and P3 depend on the *sum* through $|\mathbf{\Omega}| = |\mathbf{\Omega}^{(\mathrm{phys})}|/A_{\mathrm{u}}$, keeping the theory agnostic to the source while fully controllable in experiment.

6 Physical Interpretation of QMU Surface Parameters

To connect the Lagrangian to real materials, we interpret QMU-native surface descriptors as concrete physical properties governing geometry and dual-channel response.

Geometric and Textural Knobs

Roughness and slope. $L \equiv \mathrm{RMS}[h]/\lambda_{\mathrm{C}}$, $\quad S \equiv \mathrm{RMS}[|\boldsymbol{\nabla}_\xi h|]$. These enter through a geometry factor $\Lambda_s(L,S) = 1 + \rho_L L^2 + \rho_S S^2$, modulating thresholds and angular widths.

Magnetic flux density on the surface. $\widehat{\sigma}_{\mathrm{mflx}} \equiv \mathrm{mflx}/{\lambda_{\mathrm{C}}}^2$ is the effective magnetic-channel flux density (a magnetic "texture strength").

Magnetic flux gradient. $\widehat{g}_{\mathrm{mfxd}} \equiv \lambda_{\mathrm{C}}\,|\boldsymbol{\nabla}_\xi \ln \mathrm{mfxd}|$ measures how sharply domains vary; it is large for rapid textures (e.g., skyrmions).

Static and Dynamic Response Knobs

Aether fluctuation potential. aefp $= {e_{\mathrm{emax}}}^2/(m_{\mathrm{e}}\,{\lambda_{\mathrm{C}}}^2)$ sets a vacuum-fluctuation coupling baseline between surface wells and the Aether.

Dual-channel impedance. potn $=$ mflx $\cdot$ freq $=$ indc $\cdot$ rson $= 1/$capc. This pair governs how readily dual-charge currents establish at the surface, directly modulating Φ and dichroic response.

rmfd intensity response. mfir $= {e_{\mathrm{emax}}}^2/(m_{\mathrm{e}}\,{\lambda_{\mathrm{C}}}^3 F_{\mathrm{q}})$ quantifies how external rmfd couples into local energy density. With $\boldsymbol{\Omega} = \boldsymbol{\Omega}^{(\mathrm{phys})}/A_{\mathrm{u}}$, the combination mfir $|\boldsymbol{\Omega}|$ is the natural dimensionless drive strength at the surface.

Measurement-Facing Aggregate

Quantum efficiency. $\mathcal{Q} = \widehat{J}$ ocmp provides a ledger-native, dimensionless efficiency that compares platforms independent of external unit choices.

7 Standard predictions in QMU

Einstein line.

$$\boxed{\kappa_{\max} = u - \Phi, \qquad u_0 = \Phi} \tag{5}$$

Yield (weak drive).

$$\widehat{J} \propto \widehat{I}\,\Theta(u-\Phi)\,\Xi(u,\Phi;g_{\mathrm{e}},g_{\mathrm{m}},\lambda_{\times}). \tag{6}$$

Angular yield with CD and band.

$$\frac{\mathrm{d}\widehat{J}}{\mathrm{d}\Omega}(\widehat{\mathbf{r}}_{\xi}) \propto \Gamma_{\mathrm{em}}\,\mathcal{K}_{\mathrm{band}}(\widehat{\mathbf{r}}_{\xi};\widehat{\mathbf{d}},\vartheta_{\mathrm{C}},\varsigma_{\mathrm{C}})\,\Big[1+\mathcal{A}_{\mathrm{CD}}\cos 2(\varphi-\varphi_0)\Big]. \tag{7}$$

Polarization Dependence of the Total Yield

Let $\hat{\mathbf{n}}$ be the surface normal. Linear polarization is characterized by unit vectors $\hat{\mathbf{e}}$ (electric-channel) and $\hat{\mathbf{b}}$ (magnetic-channel) for the incident wave at the surface. From the kinetic sector $\psi^{\dagger}\mathbf{D}^2\psi$ with $\mathbf{D} = \boldsymbol{\nabla}_{\xi} - i(g_{\mathrm{e}}\,\mathbf{a}_{\mathrm{e}} + g_{\mathrm{m}}\,\mathbf{a}_{\mathrm{m}})$, the leading yield scales with the normal projections:

$$\widehat{J}_{\mathrm{tot}}(\theta_{\mathrm{pol}}) \;\propto\; (\hat{\mathbf{n}}\cdot\hat{\mathbf{e}})^2\,\underbrace{{g_{\mathrm{e}}}^2\,\Xi_{\mathrm{e}}}_{A} + (\hat{\mathbf{n}}\cdot\hat{\mathbf{b}})^2\,\underbrace{{g_{\mathrm{m}}}^2\,\Xi_{\mathrm{m}}}_{B} + (\hat{\mathbf{n}}\cdot\hat{\mathbf{e}})(\hat{\mathbf{n}}\cdot\hat{\mathbf{b}})\,\underbrace{\lambda_{\times}\,g_{\mathrm{e}}\,g_{\mathrm{m}}\,\Xi_{\times}}_{C}.$$

Let θ_{pol} be the angle of $\hat{\mathbf{e}}$ to $\hat{\mathbf{n}}$, with $\hat{\mathbf{b}} \perp \hat{\mathbf{e}}$ in the surface plane (ledger-plane convention). Then

$$\widehat{J}_{\mathrm{tot}}(\theta_{\mathrm{pol}}) \;\propto\; A\cos^2\theta_{\mathrm{pol}} + B\sin^2\theta_{\mathrm{pol}} + \tfrac{1}{2}C\sin(2\theta_{\mathrm{pol}}),$$

with A, B, C material functions fixed by §12. The extremal angles satisfy

$$\tan(2\theta_*) = \frac{C}{A-B},$$

exhibiting the *two-channel optimum* absent if $C = 0$. Since $\lambda_{\times} = \eta_{\mathrm{c}}\,\beta_0$, the displacement of θ_* from $0, \frac{\pi}{2}$ is a parameter-free prediction once $\Xi_{\mathrm{e,m,}\times}$ are calibrated.

Multi-Photon Extension (High-Drive Regime)

For strong drives, expand the source as a power series in the field invariants:

$$\Gamma_{\rm em} \;\to\; \sum_{n\geq 1} \Gamma_n \left(\mathbf{E}_{\rm e}^2 + \mathbf{B}_{\rm e}^2 + \mathbf{E}_{\rm m}^2 + \mathbf{B}_{\rm m}^2\right)^{n/2}.$$

Then the generalized Einstein line and yield scaling read

$$\boxed{\kappa_{\rm max}^{(n)} = n\,u - \Phi\ , \qquad \widehat{J}^{(n)} \propto \widehat{I}^{\,n}\,\Theta(n\,u-\Phi)}\,,$$

with the ring kernel $\mathcal{K}_{\rm band}$ retained (banded ontology) and the cone rule unchanged at fixed u. Cross-channel interference persists via $\lambda_\times$ in the angular sector, enabling n-dependent dichroic and asymmetry signatures.

8 APM/QMU predictions (P1–P3)

P1: Universal near-threshold circular dichroism. With $\chi_\Omega = \eta_{\rm c}\,\beta_0$,

$$\boxed{\mathcal{A}_{\rm CD}^{(u\approx\Phi^+)} = \eta_{\rm c}\,\beta_0 = \frac{\alpha}{2\pi} \approx 1.1614\times 10^{-3}}\,.$$

P2: rmfd work-function renormalization with surface ledger.

$$\mathrm{curl} \equiv \frac{{e_{\rm emax}}^2}{m_{\rm e}\,\lambda_{\rm C}}, \qquad \boxed{\Delta\Phi \approx -\,\beta_0\,\frac{\mathrm{curl}}{F_{\rm q}}\,\Lambda_s(L,S)\;-\;\rho_{\rm afp}\,\frac{\mathrm{aefp}}{F_{\rm q}}\,\Lambda_s(L,S)\;-\;\rho_\Omega\,\mathrm{mfir}\;|\mathbf{\Omega}|}\,,$$

All coefficients entering $\Delta\Phi$ are independently calibrated per §12; no parameters are fit on $\Delta\Phi$ itself. Physical rationale. The total shift combines (i) static channel curl, (ii) coupling to vacuum fluctuations via aefp, and (iii) direct energy-density injection from the external rotating field through the dimensionless drive mfir $|\mathbf{\Omega}|$; all are modulated by the geometric factor $\Lambda_s(L,S)$.

Harmonic content. Figure 6 isolates the 1φ front–back term characteristic of two-channel interference (P3), contrasted with the small 2φ CD ripple in Fig. 3; their product with the cardioid emboss is shown in Fig. 7.

P3: Polarization–Ring Asymmetry (two-channel signature). For prepared magnetic textures with phase lag Δ,

$$I(\varphi) \;\propto\; \mathcal{K}_{\rm band}(\cdot)\left[1 + \mathcal{A}_{\rm CD}\cos 2(\varphi-\varphi_0) + A_{\rm FB}\cos(\varphi-\varphi_{\rm f})\right],$$

with

$$\boxed{\mathcal{A}_{\rm ring} \;\simeq\; \kappa_{\rm geom}\,A_{\rm FB} \;\propto\; \lambda_\times\,\eta_{\rm c}\,\widehat{\sigma}_{\rm mflx}\,\widehat{g}_{\rm mfxd}\,\left[1+\delta_L L^2+\delta_S S^2\right]\,\cos\Delta}\,.$$

$\widehat{\sigma}_{\rm mflx}$, $\widehat{g}_{\rm mfxd}$, Λ_s *are fixed from §12;* $\mathcal{A}_{\rm ring}$ *has no adjustable surface knobs. Physical rationale.* $\mathcal{A}_{\rm ring}$ measures two-channel interference: it scales with cross coupling $\lambda_\times\eta_{\rm c}$, texture density $\widehat{\sigma}_{\rm mflx}$, and gradient sharpness $\widehat{g}_{\rm mfxd}$. Geometric roughness (L,S) enhances or suppresses the effect; Δ selects the front–back phase of the asymmetry.

9 APM Photoelectric Response Time (P4)

Statement. In QMU, time is measured by $\tau = F_{\mathrm{q}} t$. A sudden turn-on of the drive is represented by an envelope $f(\tau) = \Theta(\tau - \tau_0)$ multiplying the source term in $\mathcal{X}_\gamma$ (or the scalar potential φ). Because the evolution is first order in ∂_τ, the emission source $\mathcal{X}_\gamma$ becomes nonzero at the next quantum time tick.

Minimal response time. Define the quantum chronostep

$$\Delta\tau_{\min} = 1 \qquad \Longleftrightarrow \qquad \Delta t_{\min} = \frac{1}{F_{\mathrm{q}}}.$$

Thus the APM/QMU model predicts a finite response bounded below by $\Delta\tau_{\min} = 1$.

Derivation sketch. With $f(\tau) = \Theta(\tau - \tau_0)$ and $i\,\partial_\tau \psi = \widehat{H}[\mathbf{a}_{\mathrm{e}}, \mathbf{a}_{\mathrm{m}};\, f(\tau)]\,\psi$, Duhamel's formula yields, for $\tau > \tau_0$,

$$\psi(\tau) = U(\tau, \tau_0)\,\psi(\tau_0^-) - i \int_{\tau_0}^{\tau} U(\tau, \tau')\,\delta\widehat{H}(\tau')\,\psi(\tau')\,\mathrm{d}\tau'.$$

The exchange/source $\mathcal{X}_\gamma \propto \Gamma_{\mathrm{em}}(\cdot)\,|\psi|^2\,\mathcal{K}_{\mathrm{band}} - \Gamma_{\mathrm{abs}}(\cdot)\,|\psi|^2$ acquires a nonzero contribution at $\tau = \tau_0 + 0^+$, i.e. one QMU tick.

Prediction (P4).

$$\boxed{\textbf{P4: } \Delta\tau_{\mathrm{resp}} \geq 1 \quad (\text{equivalently } \Delta t_{\mathrm{resp}} \geq 1/F_{\mathrm{q}}).}$$

This replaces the mainstream "instantaneous" idealization with a falsifiable QMU bound. Any experiment must resolve time steps $\lesssim 1/F_{\mathrm{q}}$ to probe beyond apparent instantaneity.

10 Figures

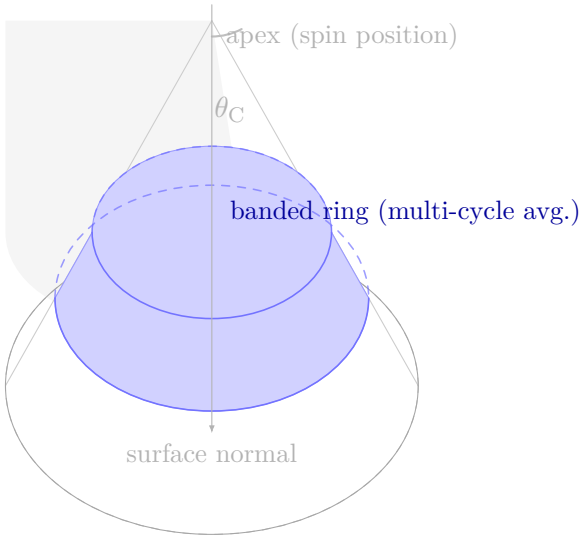

Figure 1: Shaded emission cone with banded ring (schematic geometry). The annular thickness depicts the multi-cycle averaged band produced by projecting the full loxodromic spin surface over one chronovibration. Front/back arcs are distinguished (solid vs. dashed) to indicate occlusion. The cone half-angle θ_{C} follows (C1)–(C2).

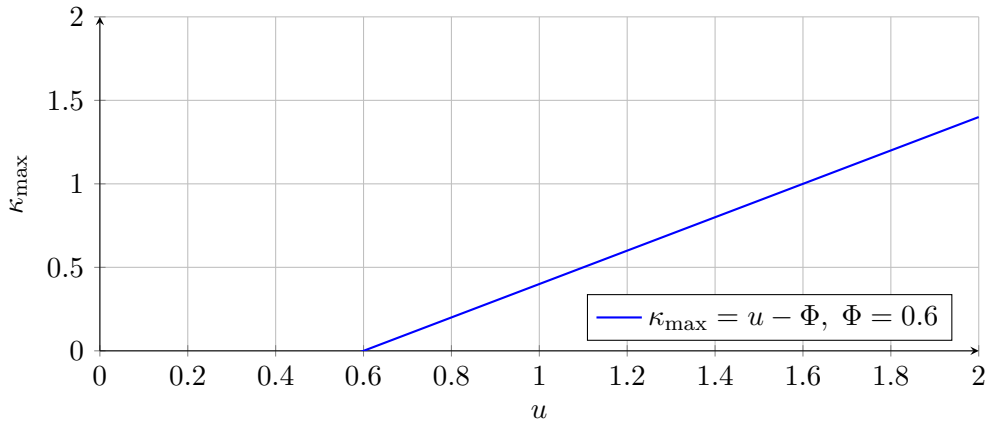

Figure 2: QMU Einstein line: exact plot of $\kappa_{\max} = u - \Phi$ with unit slope and threshold at $u = \Phi$.

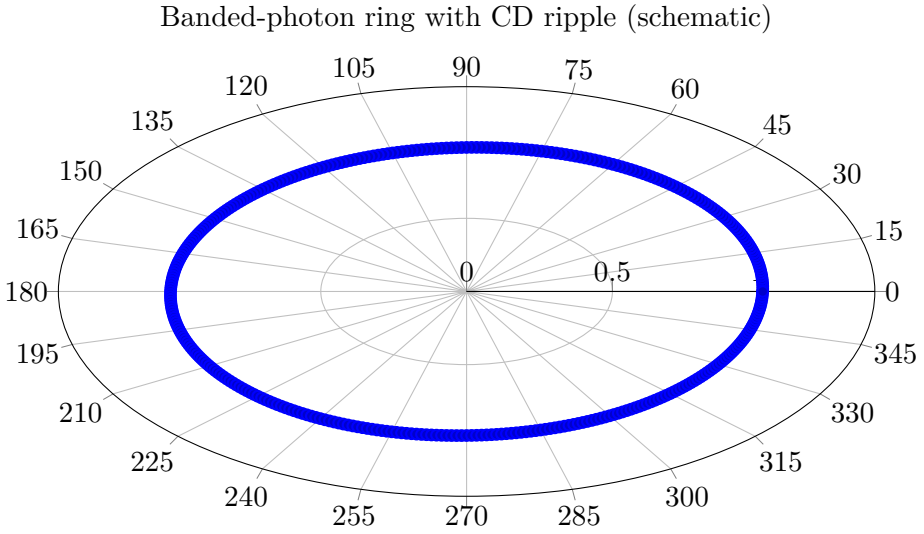

Figure 3: Ring on the observation sphere with helicity-odd 2φ modulation near threshold. Form matches Sec. “Angular yield with CD and band”; amplitude is illustrative (schematic).

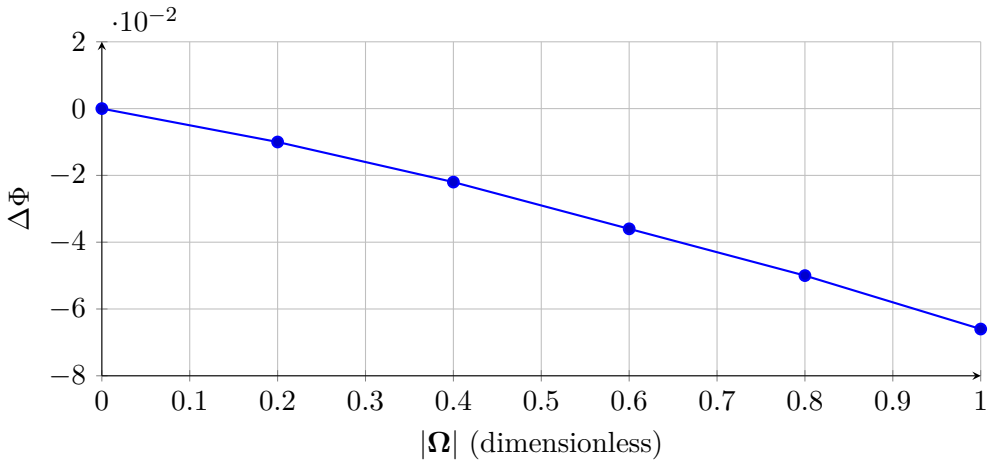

Figure 4: Rotating-field coupling with $\boldsymbol{\Omega} = \boldsymbol{\Omega}^{(\mathrm{phys})}/A_{\mathrm{u}}$ and a negative shift $\Delta\Phi$. Trend follows P2; slope here is illustrative (schematic).

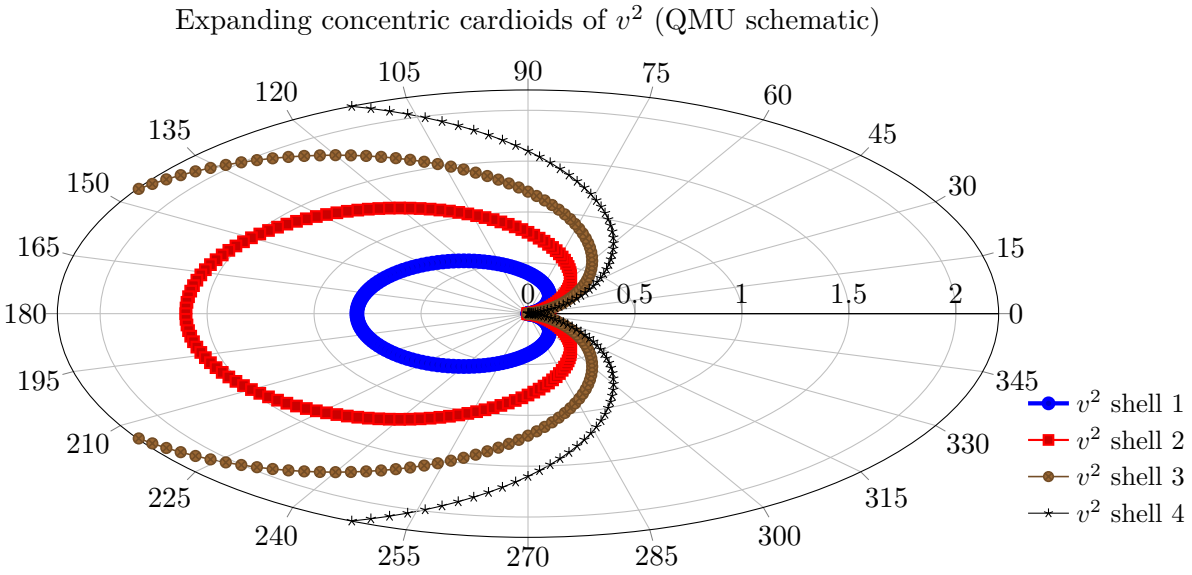

Figure 5: Concentric cardioids illustrating a QMU geometric ledger for speed-squared layers, $r(\theta) = s(1 - \cos\theta)$, exact forms; scaling s increases across shells.

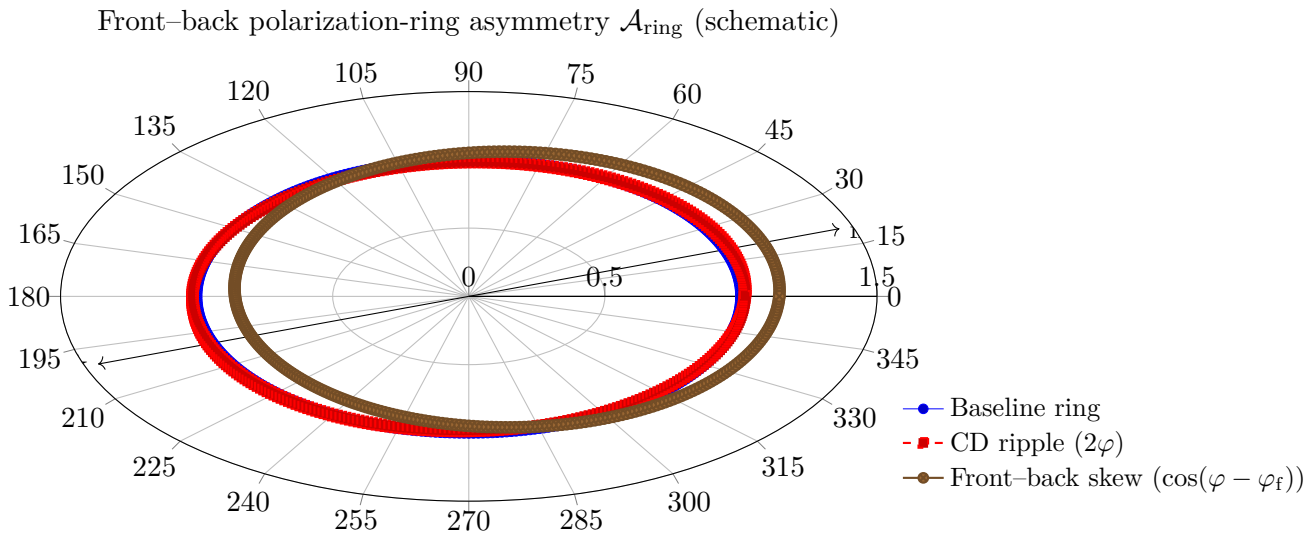

Figure 6: Visualization of $\mathcal{A}_{\mathrm{ring}}$: a first-harmonic $\cos(\varphi - \varphi_{\mathrm{f}})$ modulation (solid) produces front–back asymmetry on the banded ring. A small 2φ CD ripple (dashed) is shown for contrast. Form follows P3; amplitudes shown are illustrative (schematic).

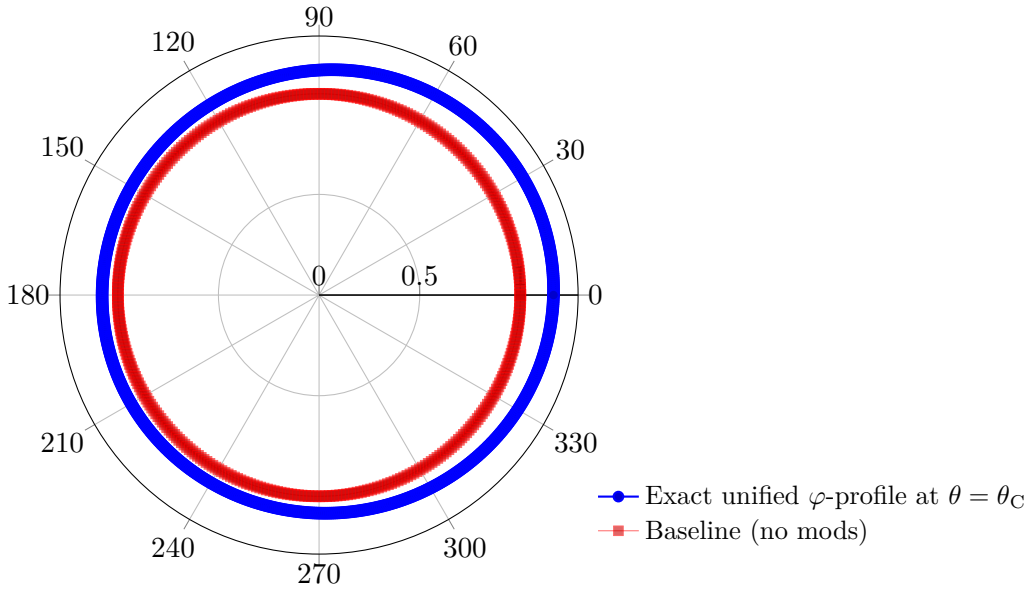

Figure 7: Unified ring intensity vs. azimuth φ at fixed $\theta = \theta_{\mathrm{C}}$: $\mathcal{J}_\Omega \propto \mathcal{K}_{\mathrm{band}}(\theta_{\mathrm{C}}; \sigma_{\mathrm{C}})\ \mathcal{C}_{\mathrm{card}}(\varphi; \varphi_0, \epsilon)\,[1 + \mathcal{A}_{\mathrm{CD}} \cos 2(\varphi - \varphi_0) + A_{\mathrm{FB}} \cos(\varphi - \varphi_{\mathrm{f}})]$. Parameters shown: $\theta_{\mathrm{C}} = 32°$ (from (C1)–(C2)), $\sigma_{\mathrm{C}} = 8°$, $\epsilon = 0.12$, $\mathcal{A}_{\mathrm{CD}} = 0.02$, $A_{\mathrm{FB}} = 0.15$, $\varphi_0 = 20°$, $\varphi_{\mathrm{f}} = 20°$. Amplitudes chosen for visibility; forms are exact.

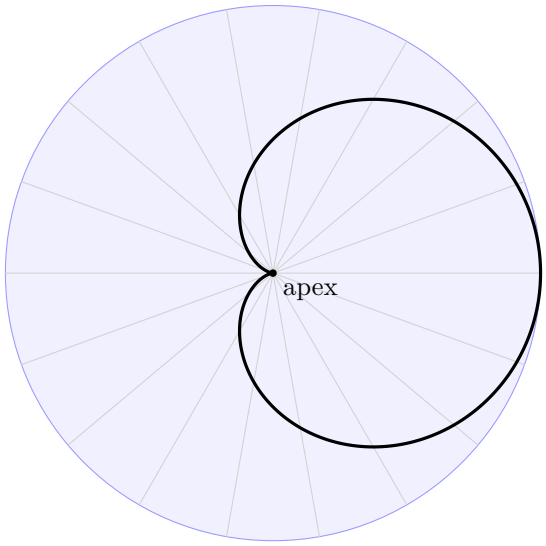

(a) Top-down cardioid in band plane.

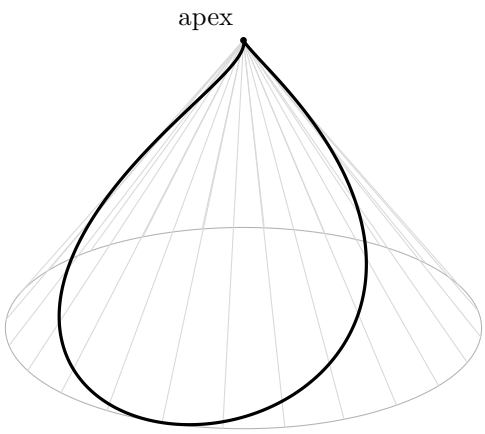

(b) Cardioid mapped on conical surface.

Figure 8: Instantaneous cardioid on the emission cone at fixed θ_{C}. (a) Top-down view shows $r(\phi) = a(1 + \cos\phi)$ with $a = \frac{R}{2}$ (so $r_{\max} = R$). (b) Exact surface embedding on a cone of height H and base radius R via $\rho = r(\phi)$ and $z = H - (H/R)\, r(\phi)$. Time-averaging over precession returns the annular band (see Fig. 1).

11 Methods and normalizations (QMU)

Field normalization and rmfd coupling. Physical rotating fields are scaled by A_{u}: $\boldsymbol{\Omega} = \boldsymbol{\Omega}^{(\mathrm{phys})}/A_{\mathrm{u}}$. Two-charge interference is controlled by $\lambda_{\times} = \eta_{\mathrm{c}}\, \beta_0$; the spin–rmfd strength uses $\chi_{\Omega} = \eta_{\mathrm{c}}\, \beta_0$.

Photon ledger (Route B). $\widehat{n}_{\gamma}$ is dynamical; continuity $\partial_{\tau}\widehat{n}_{\gamma} + \boldsymbol{\nabla}_{\xi}\cdot\widehat{\mathbf{S}}_{\gamma} = \mathcal{X}_{\gamma}$ is axiomatic via μ_{γ}. Banded emission is encoded by $\mathcal{K}_{\mathrm{band}}$ with director $\widehat{\mathbf{d}}$, cone ϑ_{C}, width ς_{C}. Rule (C1) with $\chi_{\mathrm{C}} = 1$ is the canonical baseline; (C2) tests near-threshold accentuation.

Surface descriptors in practice. We adopt $\Lambda_s(L, S) = 1 + \rho_L L^2 + \rho_S S^2$ and use $\widehat{\sigma}_{\mathrm{mflx}}$ and $\widehat{g}_{\mathrm{mfxd}}$ to parameterize magnetic texture strength and gradient. The dual-channel impedance combination potn, capc sets the material lever in $\mathcal{A}_{\mathrm{CD}}$ and $\mathcal{A}_{\mathrm{ring}}$. Quantum efficiency is evaluated as $\mathcal{Q} = \widehat{J}\,\mathrm{ocmp}$.

12 Independent Calibration of Surface-Ledger Parameters

The QMU surface descriptors in §6 are *not* free fit knobs. They admit independent, non-photoelectric calibration protocols that render P2 and P3 strictly falsifiable. We list canonically normalized (dimensionless) readouts; all drives and fields are ledger-scaled (§5).

Geometry factor $\Lambda_s(L, S)$. Obtain $L = \mathrm{RMS}[h]/\lambda_{\mathrm{C}}$ and $S = \mathrm{RMS}[|\boldsymbol{\nabla}_{\xi} h|]$ from ring-averaged speckle interferometry in reflection[10]:

$$\mathcal{C}_{\mathrm{speckle}}(\Delta\boldsymbol{\xi}) \;\to\; \{\langle h^2\rangle,\, \langle|\boldsymbol{\nabla}_{\xi} h|^2\rangle\} \quad\Rightarrow\quad \Lambda_s = 1 + \rho_L L^2 + \rho_S S^2.$$

Here ρ_L, ρ_S are *universal* geometric weights fixed once per analysis pipeline by calibration gratings in QMU.

Magnetic texture density $\widehat{\sigma}_{\mathrm{mflx}}$. Measure the ledger-normalized magnetic contrast via polarized Kerr maps[12] or spin-resolved LEED at fixed u:

$$\widehat{\sigma}_{\mathrm{mflx}} \;\equiv\; \frac{1}{2\pi}\oint_{\Gamma} \mathrm{d}\boldsymbol{\xi}\cdot(\hat{\mathbf{n}}\times\langle\mathbf{B}_{\mathrm{m}}\rangle),$$

where Γ is a microscopic loop (in $\boldsymbol{\xi}$) on the surface. This yields a ring-integrated magnetic-channel flux density independent of photoemission.

Magnetic gradient strength $\widehat{g}_{\mathrm{mfxd}}$. Extract $\widehat{g}_{\mathrm{mfxd}} = \lambda_{\mathrm{C}}\,|\boldsymbol{\nabla}_{\xi}\ln \mathrm{mfxd}|$ by differencing the previous contrast on two nested loops $\Gamma_{1,2}$ with known $\boldsymbol{\xi}$ spacing.

Dual-channel impedance (capc, potn, indc)**.** Drive the surface with a weak, broadband dual-channel probe $\{\mathbf{E}_{\mathrm{e}}(u), \mathbf{E}_{\mathrm{m}}(u)\}$ at normal incidence and read out the linear surface admittance:

$$Y_{\mathrm{QMU}}(u) \;\equiv\; \frac{J_{\mathrm{tot}}(u)}{E_{\mathrm{drive}}(u)} \;\longleftrightarrow\; \{\mathrm{capc}(u),\ \mathrm{potn}(u),\ \mathrm{indc}(u)\}$$

with the ledger identity $\mathrm{potn} = \mathrm{mflx}\cdot\mathrm{freq} = \mathrm{indc}\cdot\mathrm{rson} = 1/\mathrm{capc}$ used to cross-check consistency. This protocol uses reflectometry/ellipsometry in QMU and does not require electron detection.

Aether fluctuation potential aefp**.** Determine aefp from the low-drive, zero-angle noise floor of the surface admittance:

$$\lim_{u\to 0^{+}} \frac{\mathrm{Im}\, Y_{\mathrm{QMU}}(u)}{u} \;\propto\; \mathrm{aefp},$$

a QMU fluctuation–dissipation relation for the surface well anchored by the $\widehat{n}_{\gamma}$ sector (Route B).

rmfd intensity response mfir**.** Use a purely rotating ledger drive $\boldsymbol{\Omega}$ with vanishing linear polarization to isolate the spin–rmfd channel:

$$\delta\widehat{\mathcal{E}}_{\mathrm{surf}} \;\equiv\; \langle \tfrac{1}{2}(\mathbf{E}_{\mathrm{e}}^2+\mathbf{B}_{\mathrm{e}}^2+\mathbf{E}_{\mathrm{m}}^2+\mathbf{B}_{\mathrm{m}}^2)\rangle_{\Omega} \;\propto\; \mathrm{mfir}\,|\boldsymbol{\Omega}|.$$

This "rmfd calorimetry" returns mfir without invoking $\widehat{J}$.

With $\{\Lambda_s, \widehat{\sigma}_{\mathrm{mflx}}, \widehat{g}_{\mathrm{mfxd}}, \mathrm{capc}, \mathrm{potn}, \mathrm{aefp}, \mathrm{mfir}\}$ fixed from these protocols, the photoelectric observables in P2 and P3 involve no tunable surface parameters, providing hard falsifiability.

Table 1: Schematic error budget (dominant contributions).

Quantity	Primary confound	Mitigation / expected rel. error
$\Delta\Phi$ in P2	Temperature drift of work function	Interleaved zero-Ω runs; $<5\times10^{-3}$
$\widehat{\sigma}_{\mathrm{mflx}}$	Domain aging / hysteresis	Pre-cycle and DC tracking; $<1\times10^{-2}$
$\widehat{g}_{\mathrm{mfxd}}$	Pixel-scale point spread	Deconvolution vs. calibration grid; $<2\times10^{-2}$
Λ_s	Speckle model mismatch	Grating-based cross-check; $<5\times10^{-3}$

Table 2: Tests, observables, and suggested platforms with QMU surface knobs.

Test	Observable (QMU)	Suitable platforms	Key knobs (QMU)
E1: Einstein line	$\kappa_{\max}(u)$, threshold Φ	Clean alkali/noble; retarding-field analyzers	Tune Φ via termination (capc)
E2: CD at threshold (P1)	$\mathcal{A}_{\mathrm{CD}} = \eta_{\mathrm{c}}\,\beta_0$	CD-ARPES[5]; strong SOC crystals; chiral films	capc, potn; helicity flips
E3: rmfd drift (P2)	$\Delta\Phi \sim [\mathrm{curl} + \mathrm{aefp}]/F_{\mathrm{q}} + \mathrm{mfir}\,\lvert\boldsymbol{\Omega}\rvert$	Ferromagnets; μ-metal rigs; cold-atom surfaces	L, S (polish/etch), mfir, $\boldsymbol{\Omega}$ *(pre-calibrate §12)*
E4: Ring-resolved ARPES	$\mathrm{d}\widehat{J}/\mathrm{d}\Omega \sim \mathcal{K}_{\mathrm{band}}(\cdot)$ annulus at ϑ_{C}	Polarized crystals; oriented dipoles	Sweep u; fit $\chi_{\mathrm{C}} = 1$ baseline
E5: Single-atom axis	Hollow-cone count set by $\widehat{\mathbf{d}}$	Pumped ions/atoms	Randomize $\widehat{\mathbf{d}}$ to erase ring
E6: Polarization-ring (P3)	$\mathcal{A}_{\mathrm{ring}} \propto \lambda_{\times}\eta_{\mathrm{c}}\,\widehat{\sigma}_{\mathrm{mflx}}\,\widehat{g}_{\mathrm{mfxd}}\cos\Delta$	Skyrmion lattices; textured magnets	Texture chirality; Δ phase; L, S *(pre-calibrate §12)*

13 Experimental program (QMU readout)

14 Outlook

The same QMU/APM Lagrangian strategy extends naturally to Compton scattering (cone evolution vs u), Bremsstrahlung (two-channel radiation reaction), and atomic transitions (selection rules recast in the banded-photon ledger). With $\chi_\Omega, \lambda_\times, \lambda_{\mathrm{cplg}}, \chi_{\mathrm{C}}$ fixed by η_{c} and β_0, remaining material dependence resides in Φ_s, Ξ, Λ_s, and the surface-ledger knobs $\{\mathrm{aefp}, \widehat{\sigma}_{\mathrm{mflx}}, \widehat{g}_{\mathrm{mfxd}}, \mathrm{mfde}, \mathrm{mfir}, \mathrm{capc}, \mathrm{potn}\}$, all calibratable in QMU. Reporting the dimensionless quantum efficiency $\mathcal{Q} = \widehat{J}\,\mathrm{ocmp}$ provides a standardized ledger-native comparison across platforms, preparations, and textures.

A Appendix: Cardioid on a Cone from Aether-Unit Geometry

Setup. Let γ be the forward-time loxodromic centerline on the Aether unit sphere (constant pitch), with Frenet–Serret frame $(\mathbf{t}, \mathbf{n}, \mathbf{b})$ and polar angle $\theta(s)$, azimuth $\phi(s)$. The equal-area law $4\pi^2\, r_t\, L = \lambda_C^2$ fixes the tube radius r_t and hence the instantaneous surface density transported along γ.

Cone rule (polar selection). Stationary phase[9] along $\mathbf{t}$ picks a fixed exit polar angle $\theta = \theta_C$ ("Compton-following cone"). This is the same selection used for the banded ring; here we hold $\theta = \theta_C$ and resolve the azimuthal structure.

Azimuthal emboss from constant pitch. For a constant-pitch loxodrome, the tangent makes a fixed angle with meridians. Projecting the transported ring element onto the cone's tangent plane produces an azimuthal Jacobian

$$J(\varphi) = \mathbf{t}\cdot\mathbf{e}_\theta(\theta_C, \varphi) \;\propto\; 1 - \cos(\varphi - \varphi_0) + \mathcal{O}(\mathrm{higher}),$$

so the instantaneous intensity per unit azimuth on the cone is, to leading harmonic,

$$\mathcal{I}(\varphi) \;\propto\; \underbrace{\mathcal{K}_{\text{band}}(\theta_C)}_{\text{cone selection}}\;\underbrace{\Big[1+\epsilon\,(1-\cos(\varphi-\varphi_0))\Big]}_{\text{cardioid emboss}}, \qquad 0<\epsilon\ll 1.$$

Here $\epsilon \sim \varepsilon^2\kappa/\langle\sin\theta\rangle$ is set by the tube thickness $\varepsilon = r_t/R$, curvature scale and the projector $\mathcal{R} = \langle\sin\theta\rangle^{-1}$.

Stationary-phase exit (explicit). Let $S(\tau)$ be the local action phase along the centerline with $S'(\tau) = \text{angm}^{-1}\text{enrg} = \text{const}$ in QMU units. Construct the far-field phase $\Phi(\hat{\mathbf{r}},\tau) = \mathbf{k}\cdot\mathbf{r}(\tau) - S(\tau)$. Stationarity $\partial_\tau\Phi = 0$ gives $\hat{\mathbf{r}}\cdot\mathbf{t} = \cos\theta_C$, i.e. fixed polar angle θ_C (the cone).

First harmonic from constant pitch (lemma). A constant-pitch loxodrome has $\mathbf{t}\cdot\mathbf{e}_\phi = \text{const}$, so the Jacobian from ring transport to the cone is $J(\varphi) \propto 1-\cos(\varphi-\varphi_0) + \mathcal{O}(\text{higher})$ by the ϕ–θ linearization of the map $(\theta,\phi)\mapsto$ (cone coordinates). The leading iso-intensity contour at fixed θ_C is therefore $r(\varphi) = a[1+\cos(\varphi-\varphi_0)]$, a cardioid.

Iso-intensity contour is a cardioid. Fix a display threshold $c>0$ (or normalize by $\max_\varphi \mathcal{I}$). Writing polar coordinates in the cone's base plane, the iso-intensity contour obeys $r(\varphi) = a[1+\cos(\varphi-\varphi_0)]$ with $a \propto \epsilon\, c/\mathcal{K}_{\text{band}}(\theta_C)$, i.e.

$$\boxed{r(\varphi) = a\,(1+\cos(\varphi-\varphi_0))}$$

—the canonical cardioid. This is the instantaneous footprint; time-averaging over precession of φ_0 returns the uniform banded ring at θ_C.

Embedding on the cone. Map the base-plane cardioid to the conical surface of height H and base radius R by

$$\rho = r, \qquad z = H - \frac{H}{R}\,r, \qquad (\theta=\theta_C,\ \varphi \text{ as above}),$$

which produces the 3D "cardioid on a cone" used in Figures 8.

B QMU Glossary (Ledger-Native, with Cross-References)

m_e Electron mass (ledger base).

λ_C Quantum length (Compton wavelength), natural spatial scale.

F_q Quantum frequency (photon speed divided by λ_C); sets time via $\tau = F_\text{q}t$ (see response-time bound in Section 9).

e^2 Electrostatic channel magnitude e^2.

${e_\text{emax}}^2$ Magnetic-channel magnitude (${e_\text{emax}}^2$).

$A_\text{u} \equiv$ rmfd Aether unit; rotating magnetic field scale. Physical drives normalized as $\boldsymbol{\Omega} = \boldsymbol{\Omega}^{(\text{phys})}/A_\text{u}$ (Section 5); enters the spin–rmfd term in Equation (4).

angm Quantum of action. Identity $\text{angm} = m_\text{e}\,{\lambda_\text{C}}^2\,F_\text{q}$ (used throughout Section 2).

enrg Canonical energy scale, $\text{enrg} = \text{angm}\,F_\text{q} = m_\text{e}\,{\lambda_\text{C}}^2\,{F_\text{q}}^2$.

volm Quantum volume, $\text{volm} = {\lambda_\text{C}}^3$.

curl Channel-curl scale, $\text{curl} = {e_\text{emax}}^2/(m_\text{e}\,\lambda_\text{C})$; appears in work-function shift (P2) formula near Figure 4.

rson Resonance frequency-squared, rson $= {F_{\mathrm{q}}}^2$.

mflx Magnetic-channel flux quantum (often used as a surface density via $\widehat{\sigma}_{\mathrm{mflx}}$); features in P3 via texture knobs (see Figure 6).

aefp Aether fluctuation potential (vacuum-fluctuation coupling); contributes to $\Delta\Phi$ (see caption and text around Figure 4).

phtn Photon "impulse-flow" unit, phtn $=$ angm c.

ligt Photon throughput (light) unit, ligt $=$ phtn F_{q}; used in ocmp and quantum efficiency definitions.

ocmp Optical compliance, ocmp $= 1/$ligt; used in $\mathcal{Q} = \widehat{J}\,$ocmp (Methods/Outlook).

c Photon speed, $c = \lambda_{\mathrm{C}}\, F_{\mathrm{q}}$.

g_{e}, g_{m} Dimensionless electron couplings to electric and magnetic channels, $g_{\mathrm{e}} = e^2/$angm, $g_{\mathrm{m}} = {e_{\mathrm{emax}}}^2/$angm; enter $\mathbf{D}$ and the kinetic sector of Equation (4).

η_{c} Channel ratio, $\eta_{\mathrm{c}} = e^2/{e_{\mathrm{emax}}}^2$; appears in derived couplings (Section "Derivation of Couplings").

β_0 Canonical topological weight, $1/(16\pi^2)$; sets χ_Ω and $\lambda_\times$.

$\boldsymbol{\xi}$, τ Dimensionless space/time: $\boldsymbol{\xi} = \mathbf{r}/\lambda_{\mathrm{C}}$, $\tau = F_{\mathrm{q}}t$; used in the Lagrangian Equation (4).

u Dimensionless frequency, $u = \nu/F_{\mathrm{q}}$; appears in Einstein line and cone rules (figs. Figures 2 and 3).

κ Dimensionless kinetic energy, $\kappa = K/$enrg; see Figure 2.

Φ Dimensionless work function (binding), $\Phi = \phi/$enrg; threshold in Figure 2 and shifts in Figure 4.

$\mathbf{a}_{\mathrm{e}}$, $\mathbf{a}_{\mathrm{m}}$ Channel vector potentials (dimensionless); enter $\mathbf{D}$ and coupling structure in Equation (4).

$\mathbf{E}_{\mathrm{e}}, \mathbf{B}_{\mathrm{e}}$; $\mathbf{E}_{\mathrm{m}}, \mathbf{B}_{\mathrm{m}}$ Channel field pairs (dimensionless); appear in field kinetic terms and $\widehat{n}_\gamma$-coupling bracket of Equation (4).

$\mathbf{D}$, D_τ Covariant derivatives: $\mathbf{D} = \boldsymbol{\nabla}_\xi - i(g_{\mathrm{e}}\,\mathbf{a}_{\mathrm{e}} + g_{\mathrm{m}}\,\mathbf{a}_{\mathrm{m}})$, $D_\tau = \partial_\tau - i\,\varphi$; first line of Equation (4).

$\boldsymbol{\Omega}$ Dimensionless rmfd drive, normalized by A_{u} (Section 5); plotted in Figure 4.

$\widehat{n}_\gamma$ Dimensionless photon-number density per volm; independent field (Route B) with continuity enforced in the last line of Equation (4).

$\widehat{\mathbf{S}}_\gamma$ Dimensionless photon Poynting vector (throughput flow); in the continuity constraint of Equation (4).

$\widehat{I}$ Dimensionless photon flux along a chosen direction; used in yield scalings (Section "Standard predictions in QMU").

$\mathcal{K}_{\mathrm{band}}$ Banded-photon kernel on the observation sphere (ring at half-angle ϑ_{C}); visualized in Figure 3 and used in angular distributions.

ϑ_{C}, ς_{C}, $\widehat{\mathbf{d}}$ Cone angle, angular width, and director of the band; angle rules illustrated by Figure 3 and geometry in Figure 1.

L, S Surface roughness and slope (dimensionless); enter via $\Lambda_s(L,S)$ in P2/P3; see Figures 4 and 6 captions.

$\Lambda_s(L,S)$ Geometry factor (e.g., $1 + \rho_L L^2 + \rho_S S^2$); modulates thresholds/widths; see discussions around Figure 4 and calibration in Section 12.

$\widehat{\sigma}_{\mathrm{mflx}}$ Surface magnetic texture density; contributes to P3 amplitude (Figure 6); calibrated in Section 12.

$\widehat{g}_{\mathrm{mfxd}}$ Magnetic texture gradient strength; enhances P3 front–back asymmetry (Figure 6); calibrated in Section 12.

mfir rmfd intensity response; sets drive leverage with $|\boldsymbol{\Omega}|$ in $\Delta\Phi$ (Figure 4); calibrated in Section 12.

capc, potn, indc Dual-channel impedance trio (ledger-native), with potn $=$ mflx $\cdot$ freq $=$ indc $\cdot$ rson $= 1/$capc; used in polarization/yield modeling (Section "Polarization Dependence of the Total Yield"); calibrated in Section 12.

χ_Ω Spin–rmfd coupling, $\chi_\Omega = \eta_c\,\beta_0$; multiplies $\mathbf{\Omega}\cdot(\psi^\dagger\boldsymbol{\sigma}\psi)$ in Equation (4).

$\lambda_\times$ Electric–magnetic cross-coupling, $\lambda_\times = \eta_c\,\beta_0$; appears in field sector of Equation (4) and drives $\mathcal{A}_{\text{ring}}$ (Figure 6).

λ_{cplg} Photon–field coupling in the $\widehat{n}_\gamma$ bracket; set to 1 by ledger normalization in Equation (4).

χ_C Cone-rule constant (= 1); sets the Compton-following band in ring plots (Figure 3) and the cone in Figure 1.

$\mathcal{A}_{\text{CD}}$ Circular-dichroism amplitude (helicity-odd 2φ harmonic); shown in Figure 3.

$\mathcal{A}_{\text{ring}}$ Front–back ring asymmetry ($\cos\varphi$ skew); visualized in Figure 6.

$\mathcal{Q}$ Quantum efficiency: $\mathcal{Q} = \widehat{J}\,\text{ocmp}$; reported as a ledger-native, dimensionless comparator (Methods/Outlook).

Acknowledgments

D.W.T. III thanks colleagues at the Quantum AetherDynamics Institute for discussions and feedback. Constructive drafting and editorial assistance were provided by large-language-model tools, including OpenAI's ChatGPT and Google's Gemini. Any remaining errors are the author's own.

References

[1] A. Einstein, "Über einen die Erzeugung und Verwandlung des Lichtes betreffenden heuristischen Gesichtspunkt," *Annalen der Physik* **17**, 132–148 (1905).

[2] R. A. Millikan, "A Direct Photoelectric Determination of Planck's h," *Physical Review* **7**, 355–388 (1916).

[3] A. H. Compton, "A Quantum Theory of the Scattering of X-Rays by Light Elements," *Physical Review* **21**, 483–502 (1923).

[4] A. Damascelli, Z. Hussain, and Z.-X. Shen, "Angle-resolved photoemission studies of the cuprate superconductors," *Reviews of Modern Physics* **75**, 473–541 (2003).

[5] M. Hoesch and J. Henk, "Spin-polarized photoemission and circular dichroism in angle-resolved photoemission spectroscopy," *Journal of Physics: Condensed Matter* **31**, 013001 (2018).

[6] N. Nagaosa and Y. Tokura, "Topological properties and dynamics of magnetic skyrmions," *Nature Nanotechnology* **8**, 899–911 (2013).

[7] A. L. Cavalieri *et al.*, "Attosecond spectroscopy in condensed matter," *Nature* **449**, 1029–1032 (2007).

[8] M. Schultze *et al.*, "Delay in Photoemission," *Science* **328**, 1658–1662 (2010).

[9] N. Bleistein and R. A. Handelsman, *Asymptotic Expansions of Integrals*, Dover (1975).

[10] J. W. Goodman, *Speckle Phenomena in Optics: Theory and Applications*, Roberts & Company (2007).

[11] R. Kubo, "The fluctuation-dissipation theorem," *Reports on Progress in Physics* **29**, 255–284 (1966).

[12] Z. Q. Qiu and S. D. Bader, "Surface magneto-optic Kerr effect," *Review of Scientific Instruments* **71**, 1243–1255 (2000).

[13] J. D. Jackson, *Classical Electrodynamics*, 3rd ed., Wiley (1999).